Volume 8
Number 3
21 January 2020
Pages 823–1490

Journal of Materials Chemistry A

Materials for energy and sustainability

rsc.li/materials-a

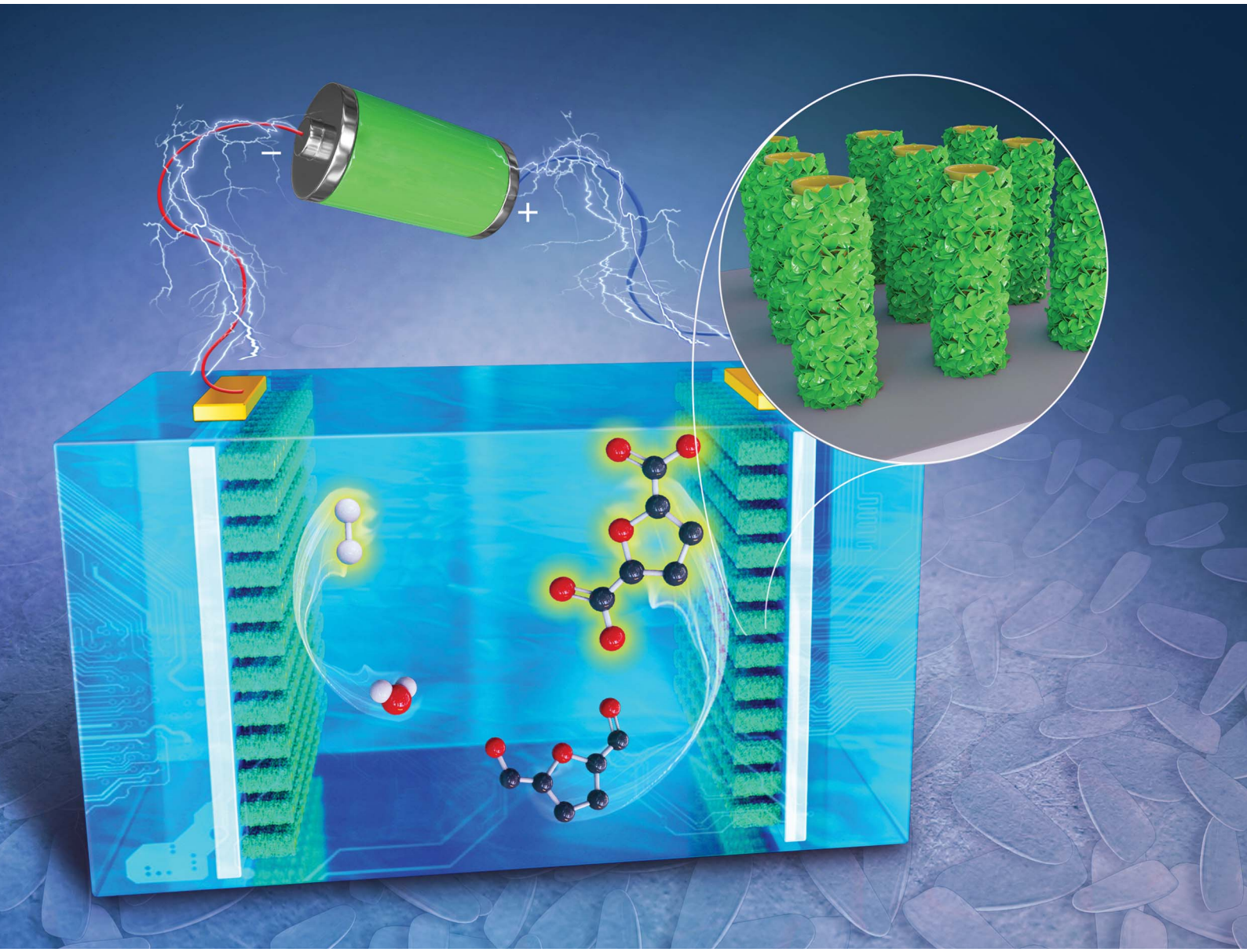

ISSN 2050-7488

ROYAL SOCIETY OF CHEMISTRY

PAPER

Xian-Zhu Fu, Jing-Li Luo *et al.*

Coupling efficient biomass upgrading with H_2 production *via* bifunctional Cu_xS@NiCo-LDH core–shell nanoarray electrocatalysts

Journal of Materials Chemistry A

PAPER

View Article Online
View Journal | View Issue

Cite this: J. Mater. Chem. A, 2020, 8, 1138

Coupling efficient biomass upgrading with H_2 production *via* bifunctional Cu_xS@NiCo-LDH core–shell nanoarray electrocatalysts†

Xiaohui Deng,[a] Xiaomin Kang,[a] Mei Li,[a] Kun Xiang,[a] Cheng Wang,[a] ZaiPing Guo,[b] Jiujun Zhang,[c] Xian-Zhu Fu *[a] and Jing-Li Luo *[ad]

Received 27th June 2019
Accepted 12th September 2019

DOI: 10.1039/c9ta06917h

rsc.li/materials-a

To boost hydrogen production from water splitting, the electrochemical oxidation of biomass-derived molecules to produce valuable chemicals is regarded as a promising approach to replace the kinetically sluggish oxygen evolution reaction. Herein, copper sulfide nanowire@NiCo-layered double hydroxide (LDH) nanosheet core–shell nanoarrays are fabricated as efficient bifunctional electrocatalysts for 5-hydroxymethylfurfural (HMF) oxidation and water reduction to simultaneously produce value-added 2,5-furandicarboxylic acid (FDCA) and hydrogen fuel with less energy consumption. Benefiting from the fast charge transfer induced by the Cu_xS core, the Co/Ni interaction in the LDH nanosheet layer and the open nanostructure, the optimized catalysts exhibit superior electrocatalytic activity (record-high 87 mA cm^{-2} @ 1.3 V *vs.* RHE for HMF oxidation; $\eta = 107$ mV @ 10 mA cm^{-2} for HER) and durability; the faradaic efficiency towards FDCA and H_2 is close to unity. The bifunctional two-electrode electrolyzer only requires a low voltage of 1.34 V to co-generate H_2 and FDCA at 10 mA cm^{-2}. This work highlights the significance of tuning the redox properties of transition metals and constructing nanoarray electrocatalysts towards more efficient energy utilization.

1. Introduction

In the ongoing worldwide exploration of clean energy, hydrogen (H_2) is regarded as a promising candidate fuel which could be produced by electrochemical water splitting.[1–4] However, the oxygen evolution reaction (OER) has been considered as the bottleneck of overall water splitting since it suffers from a high overpotential and sluggish kinetics.[5] Moreover, since O_2 is of limited value and the mixing of O_2 with H_2 gives rise to potential safety issues, it is highly desirable to replace OER with novel oxidation processes that are kinetically favorable and meanwhile, capable of producing valuable chemicals.[6–8] For instance, the oxidation of hydrazine, urea, and methanol, and sulfur generation have been coupled with cathodic H_2O reduction to effectively reduce energy consumption towards H_2 generation.[9–12]

Recently, the oxidation of 5-hydroxymethylfurfural (HMF) has attracted considerable attention.[6,13–17] As one of the most widely studied biomass-derived platform molecules, it is in great abundance and can be upgraded to chemicals such as 5-diformylfuran (DFF), 5-hydroxymethyl-2-furancarboxylic acid (HMFCA), maleic anhydride (MA) and 2,5-furandicarboxylic acid (FDCA). In particular, FDCA is gaining intense interest as it can act as the monomer towards synthesis of renewable polymer materials.[18] Compared with the traditional catalysis approach that utilizes noble metal catalysts and requires high reaction temperature, electrochemical oxidation of HMF can be performed under benign conditions without using expensive oxidants.[19,20] 2,2,6,6-Tetramethyl-1-piperidinyloxy (TEMPO) has been reported as a redox mediator to facilitate HMF oxidation in a photoelectrochemical cell.[21] Sulfide and phosphide of Ni can act as efficient electrocatalysts for HMF oxidation and the reaction occurs at a significantly lower voltage (~200 mV) compared with OER.[6,13,14] Moreover, the reaction is highly selective and the faradaic efficiency towards FDCA production is above 97%.

The Ni catalyzed oxidation of alcohols, aldehydes and primary amines has been proposed to follow the pathway in which Ni^{2+} is oxidized to NiOOH in the first step, and then the formed NiOOH would chemically oxidize organic functional groups and cycle back to lower oxidation states.[22,23] Recent *in situ* Raman studies and the appearance of surface (oxy) hydroxide species after long-term catalysis also support this

[a]College of Materials Science and Engineering, Shenzhen University, Shenzhen, 518060, China. E-mail: xz.fu@szu.edu.cn

[b]Institute for Superconducting and Electronic Materials, School of Mechanical, Materials, Mechatronic and Bio-medical Engineering, University of Wollongong, NSW 2500, Australia

[c]Institute for Sustainable Energy, College of Sciences, Shanghai University, Shanghai, 200444, China

[d]Department of Chemical and Materials Engineering, University of Alberta, Edmonton, Alberta T6G 1H9, Canada. E-mail: Jingli.luo@ualberta.ca

† Electronic supplementary information (ESI) available. See DOI: 10.1039/c9ta06917h

reaction pathway.[7,24] Due to the reason that NiOOH is a necessary prerequisite towards further oxidation reactions, the onset potential of monometallic Ni-based electrocatalysts is often limited to ~1.36 V *vs.* RHE regardless of the target functional groups, and we, therefore, anticipate that tuning the redox behavior of Ni could negatively shift its oxidation potential and further enhance the H_2 production efficiency.[25] Furthermore, despite the fact that the construction of nanostructures is rarely targeted in this field, we consider the exposure of active sites and the mass transfer as the critical factors towards high catalytic performance since the chemical oxidation step occurs directly between the exposed NiOOH species and surface-adsorbed organic substrates.[26]

Herein, we report the facile preparation of copper sulfide nanowire@NiCo-layered double hydroxide nanosheet core–shell (Cu_xS@NiCo-LDH) nanoarrays as efficient bifunctional electrocatalysts towards simultaneous HMF oxidation and H_2 evolution. By facilitating charge/mass transfer with Cu_xS core–NiCo-LDH shell nanostructures and tuning the electronic structure of Ni with Co, the onset potential towards HMF oxidation is negatively shifted by ~150–200 mV compared with the typical literature value of ~1.36 V *vs.* RHE, and a current density of 87 mA cm^{-2} is achieved at 1.3 V *vs.* RHE with a faradaic efficiency of nearly 100% for FDCA production. The core–shell nanoarray electrocatalysts also show outstanding hydrogen evolution activity/durability. Moreover, the electrolyzer with Cu_xS@NiCo-LDHs as bifunctional electrocatalysts only requires a low voltage of 1.34 V to achieve the current density of 10 mA cm^{-2}, which illustrates their superior bifunctionality in transition metal-catalyzed biomass upgrading coupled with H_2 production.

2. Experimental

2.1 Materials

Preparation of Cu_xS nanoarrays (NAs) supported on copper foam (CF). The copper foam was ultrasonicated sequentially with ethanol, 3 M HCl aqueous solution and deionized water (DIW) for 5 min. Then the CF was rinsed with DIW and subsequently immersed in static 2 M NaOH/0.11 M APS aqueous solution for chemical oxidation. The color of CF changed gradually to light blue, indicating the formation of $Cu(OH)_2$ and it was then thoroughly rinsed with DIW after 15 min. Lastly, the foam was dried at 60 °C in air. The transformation from $Cu(OH)_2$ NAs/CF to Cu_xS NAs/CF was conducted at room temperature by a sulfidation treatment in 0.1 M Na_2S aqueous solution (overnight). The final product was rinsed with DIW and dried at room temperature.

Electrodeposition of NiCo LDH on Cu_xS NAs/CF. The deposition of nickel cobalt layered double hydroxide on Cu_xS nanoarrays was conducted by electrodeposition from an aqueous solution of nitrate precursors. The ratio of transition metals was tuned by varying the precursor amounts and the total concentration of nitrates was fixed to 0.05 M. The electrodeposition was performed in a three-electrode configuration, with Cu_xS NAs/CF as the working electrode, a Pt sheet as the counter electrode and a saturated calomel electrode (SCE) as the reference electrode. The deposition potential was −1.0 V *vs.* SCE and the optimized deposition time was 450 s. The composite electrode was then rinsed with DIW and dried under ambient conditions.

2.2 Electrochemical measurements

The linear scans of electrochemical hydrogen evolution, oxygen evolution and 5-HMF oxidation reactions were conducted on a CHI760e potentiostat with a three-electrode configuration. The as-prepared composite/CF (0.5 × 0.5 cm^2) was used as the working electrode and the Hg/HgO electrode was used as the reference electrode. A 1 × 1 cm^2 Pt sheet was used as the counter electrode in OER and 5-HMF oxidation while a graphite rod was used in the case of HER to avoid potential contamination due to the Pt dissolution and deposition on the working electrode. 1 M KOH (pH 13.8) with or without the presence of 10 mM HMF was used as the electrolyte and the linear scans were collected with a scan rate of 5 mV s^{-1}. For the oxidation of HMF, the working electrode was pre-conditioned by cycling between 0.6 and 1.5 V with a scan rate of 50 mV s^{-1} until a stable voltammogram was obtained. In order to identify current contributions from catalyst oxidation, OER and HMF oxidation, the electrodes were first tested in 1 M KOH electrolyte without the presence of HMF, afterwards, a certain amount of HMF was added to achieve a concentration of 10 mM and linear scans were collected. The electrochemical impedance spectroscopy measurements were carried out in the same configuration with a cathodic potential of −1.1 V *vs.* Hg/HgO. The spectra were collected in a frequency range of 0.1 to 10^5 Hz with an amplitude of 5 mV. The ohmic drop was determined from electrochemical impedance spectroscopy and was compensated manually.

The constant potential oxidation of HMF was conducted with a Solartron SI1287 potentiostat and the *IR* drop was compensated automatically in the current interrupt mode (off time 27 μs, on/off ratio 255) to maintain the potential applied on the working electrode. The stability of Cu_xS@$Ni_{0.75}Co_{0.25}O_xH_y$ towards HMF oxidation was evaluated by chronoamperometry at 1.32 V *vs.* RHE in 10 mL 1.0 M KOH with 10 mM HMF for five successive trials. For the HER stability test, the potential to reach a current density of 10 mA cm^{-2} was monitored for 20 h. For the two-electrode electrolyzer, Cu_xS@$Ni_{0.75}Co_{0.25}O_xH_y$/CF was employed as the cathode and anode.

2.3 Characterization and product quantification

The morphologies were characterized by field-emission scanning electron microscopy (FESEM, SU-70) and field-emission transmission electron microscopy (FETEM, JEM-3200FS). X-ray diffraction (XRD) patterns were recorded using a Bruker D8 Advance (Cu Kα, 50 kV and 360 mA). X-ray photoelectron spectroscopy (XPS) was performed on a PHI5000 VersaProbe and all the peaks were calibrated with the C 1s spectrum at a binding energy of 284.8 eV. For ICP-OES measurements, the materials were collected from the electrodes by sonication and centrifugation. Then, the powders were dissolved in aqua regia

and diluted with DIW. The liquid was then analyzed with an Agilent 720. To measure the leaching losses of metal species after HER and HMF oxidation, the experiments were conducted in a two-compartment electrochemical cell separated by a Nafion 117 membrane. The electrolytes were collected, filtered and neutralized with HCl solution before being analyzed by ICP-OES. The H_2 produced from the cathodic reaction was identified by gas chromatography (Agilent 7890A) analysis and the amount generated was determined with the water displacement method.

The identification and quantification of 5-HMF and oxidation products were performed by high-performance liquid chromatography (HPLC) on a Shimadzu Prominence-I LC 2030 Plus at room temperature. After a certain number of charges were passed, 20 μL of the electrolyte solution was withdrawn and diluted with 980 μL DIW. The HPLC was equipped with a Shimadzu Shim-pack GIST column (5 μm C18, 4.6 × 250 mm) and a UV-VIS detector set at $\lambda = 265$ nm. A mixture of 70% 5 mM ammonium formate aqueous solution and 30% methanol was used as the eluent. An injection volume of 10 μL was applied and the identification/determination of the concentration of reactants/oxidation products were achieved from calibration curves of known concentrations of commercially purchased compounds.

The conversion (%) of 5-HMF and the yield (%) of oxidation products were calculated based on the following equations:

$$\text{Conversion}\ (\%) = \frac{\text{mole of substrate consumed}}{\text{initial mole of substrate}} \times 100\%$$

$$\text{Yield}\ (\%) = \frac{\text{mole of product produced}}{\text{initial mole of substrate}} \times 100\%$$

The faradaic efficiency (FE) of product formation was calculated based on the following equation:

$$\text{FE}\ (\%) = \frac{\text{mole of product produced} \times n \times F}{\text{total charge passed}} \times 100\%$$

where n is the number of electrons transferred for each product formation and F is the Faraday constant (96 485 C mol^{-1}).

$$\text{FE}\ (\%) = \frac{\text{mole of product produced} \times n \times F}{\text{total charge passed}} \times 10$$

2.4 Computational method

The density of states calculations were performed by using the Vienna *Ab initio* Simulation Package (VASP), employing the density functional theory (DFT) and the Projected Augmented Wave (PAW) method.[27–29] The Perdew–Burke–Ernzerhof (PBE) functional was used to describe the exchange and correlation effect.[30] For all the geometry optimizations, the cutoff energy was set to be 450 eV. Spin polarization was included in all the cases. The GGA+U calculations were performed using the model proposed by Dudarev *et al.*, with the U_{eff} (U_{eff} = Coulomb U − exchange J) values of 3.3 eV and 6.4 eV for Co and Ni, respectively.[31] The energy and force convergence tolerances were set to be 10^{-5} eV and 0.01 eV Å^{-1}, respectively.

3. Results and discussion

The preparation of Cu_xS@NiCo-LDH core–shell nanoarrays is illustrated in Fig. 1a. Briefly, the $Cu(OH)_2$ nanowire arrays (NAs) are first fabricated from commercially available Cu foam (Fig. S1a–c†). Afterwards, the $Cu(OH)_2$ NAs are immersed in Na_2S aqueous solution and the ion exchange process occurring at room temperature leads to the formation of Cu_xS NAs. The SEM images (Fig. S1d–f†) show that the nanowire morphology is well preserved after the sulfidation step while a slight increase of the diameter of nanowires (~30 nm) can be observed, which is attributed to the increased surface roughness during the sulfide formation.[32] A Cu to S ratio of close to 2 is obtained from the elemental analysis (Fig. S1g–i and Table S1†) and the XRD pattern (Fig. S2a†) suggests the dominant presence of metallic Cu (substrate), $Cu_{31}S_{16}$ and Cu_2O (trace mount). Since the copper sulfide polymorphs (*e.g.*, Cu_9S_5, $Cu_{7.2}S_4$ and Cu_2S) exhibit reflections at similar positions, the copper sulfide in this work is referred to as Cu_xS. In the final step, the NiCo-LDHs are coated on the Cu_xS NAs by electrodeposition.

The morphology of synthesized Cu_xS@NiCo-LDHs is then characterized by scanning electron microscopy (SEM). As shown in the SEM images (Fig. 1b–d and S3†), all the composite materials (with various Ni to Co ratios) show well-aligned nanoarrays coated by a 3D nanosheet-assembled porous nanostructure. Due to the nature of metal cations, the detailed structure of hydroxide species varies depending on the precursor composition.[33] The porosity of deposited LDHs and vertically aligned nanoarrays could expose a large number of active sites and provide low-resistant pathways for the electrolytes and reactants, thus facilitating the mass transfer of the reactive species. The chemical composition of electrodeposited species is analyzed by ICP-OES and the Ni to Co ratio is in good

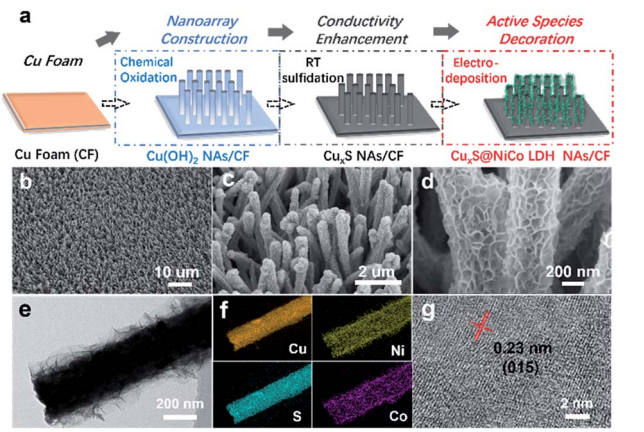

Fig. 1 (a) Schematic illustration of the preparation of Cu_xS@NiCo-LDHs core–shell composites. (LDH for layered double hydroxide, NA for nanoarrays, and RT for room temperature). (b–d) SEM images, (e) TEM image, (f) Elemental mappings of Cu_xS@$Ni_{0.75}Co_{0.25}O_mH_n$. (g) HRTEM image of ultra-thin $Ni_{0.75}Co_{0.25}$-LDH.

agreement with the anticipated values (Table S2†). Fig. 1b–d show the SEM images of the sample with a Ni to Co ratio of 3. The core–shell nanoarray structure is homogeneously distributed on the copper foam, and the TEM image (Fig. 1e) shows that Cu_xS nanowires with a diameter of ~260 nm are uniformly coated by the LDH nanosheets. Elemental mappings (Fig. 1f) confirm that Cu and S are dominantly located on the Cu_xS nanowires while Ni and Co are uniformly distributed on the nanosheets in the outer-shell. The HRTEM image (Fig. 1g) shows lattice fringes with the interplanar spacing of 0.23 nm, which could be assigned to the (015) planes of NiCo-LDH. The XRD patterns of as-prepared Cu_xS@NiCo LDHs were also collected and the reflections which can be assigned to the (110) plane of the LDH phase are marked in Fig. S2b.† Due to the ultrathin morphology and low content, the intensities of the characteristic reflections are quite weak.

The room-temperature sulfidation step is essential for the successful preparation of the core–shell structure as the metallic character of Cu_xS would provide sufficient electrical conductivity for the electrodeposition and more importantly, be beneficial for the transfer of charge carriers in further electrochemical applications.[34–36] This key aspect is also highlighted elsewhere in the Cu_xS@NiFe LDH core–shell nanoarrays towards overall water splitting where the Cu core provides good electronic transport.[37] However, in their report, the transformation of $Cu(OH)_2$ NAs to Cu involves a high energy consumption step (calcination at 180 °C for 1 h) followed by an electrochemical reduction procedure. In this work, the overall preparation protocol is significantly simplified and much less energy-consuming as the sulfidation step occurs at room temperature in aqueous solution and the reduction by electricity or any other reductant is not necessary. Furthermore, the readily maintained nanoarray structure would greatly facilitate the mass transfer involved in electrochemical processes.[38] Therefore, this low-cost, all solution-based synthesis protocol could potentially provide guidance for large-scale manufacture of highly active electrocatalysts. In the control experiment, the electrodeposition of LDHs on pristine $Cu(OH)_2$ NAs is not feasible and results in large areas where LDHs are not deposited due to their poor conductivity (Fig. S4†).

The electrocatalytic performance of as-prepared Cu_xS@NiCo-LDHs towards HMF oxidation is evaluated under alkaline conditions. The linear scans (OER and HMF oxidation after addition of 10 mM HMF) of $Cu_xS@NiO_mH_n$ and $Cu_xS@CoO_mH_n$ are presented in Fig. 2a and b. It can be observed that compared with OER, in the case of Ni, the anodic current of HMF oxidation follows the $Ni(OH)_2$/NiOOH oxidation couple in a lower potential range but with significantly enhanced current density at potentials exceeding 1.4 V. The reason is that the NiOOH generated from the oxidation of $Ni(OH)_2$ acts as the chemical oxidant towards HMF oxidation and in this way, the $Ni(OH)_2$ species are regenerated and therefore more charges are passed during the anodic scan.[22] Recently, a new mechanism has been proposed for HMF oxidation on a nickel electrode that at higher oxidation potentials, HMF could be directly oxidized by NiOOH without involving the transformation of NiOOH to $Ni(OH)_2$.[15] However, this phenomenon is only present on thin

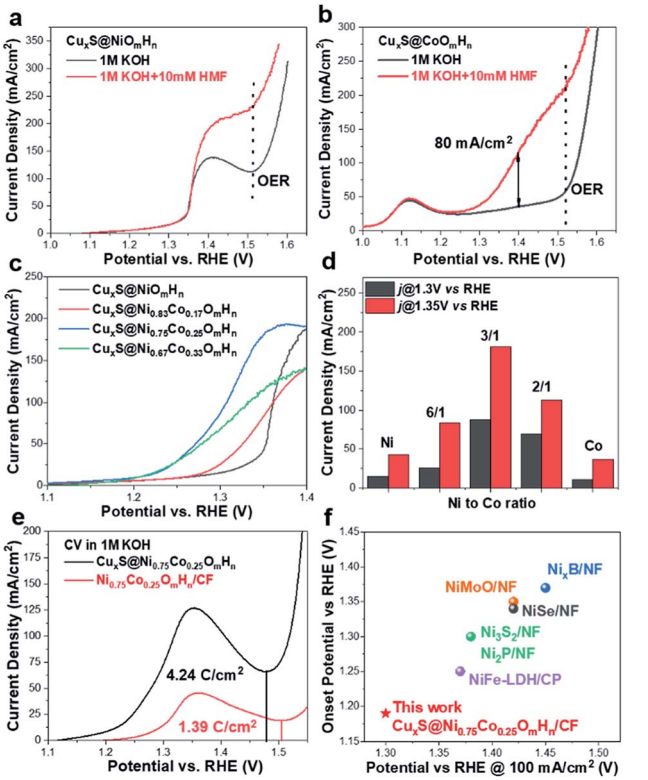

Fig. 2 (a and b) LSV curves of $Cu_xS@NiO_mH_n$ and $Cu_xS@CoO_mH_n$ towards electrochemical HMF oxidation. (c) Comparison of LSV curves of Cu_xS@NiCo LDHs with various Ni to Co ratios. (d) Current densities of prepared electrodes at 1.3 V and 1.35 V *vs.* RHE. (e) CV curves of $Cu_xS@Ni_{0.75}Co_{0.25}O_mH_n$, $Ni_{0.75}Co_{0.25}O_mH_n$/CF in 1 M KOH and calculated charges for the oxidation of transition metal cations prior to the oxygen evolution reaction. (f) Performance comparison of Cu_x-S@$Ni_{0.75}Co_{0.25}O_mH_n$ with reported electrocatalysts towards electrochemical oxidation of HMF, urea and primary amine.

film electrodes and not observed in our experiments, probably due to the high current densities. As is shown, $Cu_xS@NiO_mH_n$ exhibits anodic current densities of 42.3 mA cm^{-2} and 187.4 mA cm^{-2} at 1.35 V and 1.4 V *vs.* RHE, respectively, and such performance is comparable to those of the recently reported benchmark electrocatalysts (NiFe LDH, Ni_2P@NF, and Ni_3S_2@NF) towards HMF oxidation (Table S3†),[6,13,17] while in the case of electrodeposited Co, the position and current of the oxidation peak (Co^{2+}/Co^{3+}) at 1.13 V *vs.* RHE are nearly identical regardless of the presence of HMF, indicating that the formed CoOOH is not able to chemically oxidize HMF efficiently.[15] Interestingly, the sample exhibits an additional anodic current when the potential exceeds 1.23 V *vs.* RHE in comparison with that measured under OER conditions, illustrating the direct oxidation of HMF. It is worth mentioning that the Cu_x-S@$Co(OH)_2$ shows the lowest onset potential (1.23 V *vs.* RHE) compared with the recently reported Co-based electrocatalysts for HMF oxidation (Co-P/CF, 1.3 V *vs.* RHE; CoB/NF, ~1.32 V *vs.* RHE).[14,39] Furthermore, it exhibits a current density of 80 mA cm^{-2} at 1.4 V *vs.* RHE, which is significantly higher than that of the aforementioned counterparts (Table S3†). The superior catalytic activity of $Cu_xS@Co(OH)_2$ is attributed to the

nanowires@nanosheet core–shell array architecture and a large number of exposed active sites.

Since the redox behavior of transition metals can be tuned by the incorporation of secondary species, it is then intriguing to investigate the activity of NiCo-LDHs.[25,40] The OER polarization curves and the anodic scans in the presence of 10 mM HMF of all the mixed composites are plotted in Fig. S5.† As can be observed, all samples exhibit an enhanced anodic current before the onset of OER when HMF is present, suggesting the activity for HMF oxidation. The linear scans in 1 M KOH + 10 mM HMF are then compared and plotted in Fig. 2c. Due to the reason that under higher potentials, the mass transport of HMF under such concentration (10 mM) may hinder the overall process, the potential range of the plot is chosen between 1.1 V and 1.40 V *vs.* RHE. As is shown, the onset potential is clearly negatively-shifted compared with $Cu_xS@NiO_mH_n$ and this indicates that the HMF oxidation catalyzed by $Cu_xS@NiCo$-LDHs occurs with less energy consumption. The Ni/Co ratio of 3 is shown to be the optimal composition. It can be observed from the linear scan comparison (Fig. 2c) that the Co content in the mixed LDH is critical to induce the decrease of onset potential as the electrodes with the lowest amount of Co (Ni/Co = 5) show the slightest performance enhancement. Further increasing the Co content to Ni/Co = 3 and 2 shifts the onset potential to a nearly identical value (~1.18 V *vs.* RHE) and this indicates that an additional amount of Co has a negligible impact on the onset potential towards HMF oxidation after the optimal scenario. Meanwhile, the Ni content is another important parameter as we speculate that Ni acts as the dominant active species in the mixed LDHs (see the following discussion) and an excess amount of Co decreases the content of electrochemically active nickel species in the LDH and is therefore detrimental to the overall catalytic activity. To be more specific, the optimized electrode (with a Ni/Co ratio of 3) exhibits current densities of 87 mA cm^{-2} and 180.6 mA cm^{-2} at 1.3 V and 1.35 V *vs.* RHE, respectively, which are 5.8 and 4.3 times higher than that of $Cu_xS@NiO_mH_n$ and also significantly greater than those of the other counterparts (Fig. 2d). The Co incorporation also shows an influence on the reaction kinetics. As plotted in Fig. S6,† the $Cu_xS@NiO_mH_n$ displays a Tafel slope of 27 mV dec^{-1}, indicating the fast kinetics of $Ni(OH)_2$ being oxidized to NiOOH. On the other hand, the Tafel slopes are around ~85 mV dec^{-1} for all Co-containing samples regardless of the cobalt concentration. The advantage of the core–shell nanoarray structure is clearly demonstrated when compared with the films directly deposited on copper foam. As shown in Fig. S7,† due to the relatively smaller surface area of untreated CF, the deposited electrode shows thick films with multiple cracks. To straightforwardly compare the quantity of electrochemically active species on the electrode surface, the charge consumed by the oxidation of transition metal cations is calculated from the integration of oxidation peaks as shown in the CVs (Fig. 2e). As calculated, $Cu_xS@Ni_{0.75}Co_{0.25}O_mH_n$ exhibits a total anodic charge of 4.24 C cm^{-2} prior to the oxygen evolution reaction, which is ~3 times higher than that of $Ni_{0.75}Co_{0.25}O_mH_n$ deposited on copper foam (1.39 C cm^{-2}) and this suggests greatly increased electrochemically active species in the core–shell nanoarray electrocatalyst. As a result, the catalytic activity towards HMF oxidation is substantially higher (Fig. S7†). It should be further highlighted that $Cu_xS@Ni_{0.75}Co_{0.25}O_mH_n$ LDHs can be considered as the most active catalysts towards electrochemical HMF oxidation reported so far (Fig. 2f) since the lower onset potential (1.19 V *vs.* RHE) and the significant oxidation current at potentials more negative than 1.3 V *vs.* RHE represent a remarkable advance in this field. Recently, the electro-oxidation of urea and amine catalyzed by Ni-based electrocatalysts (NiMoO/NF and NiSe/NF, Fig. 3d) has also been studied and the *in situ*/*ex situ* characterization proved that such reactions follow a similar pathway to Ni-catalyzed HMF oxidation.[7,41] Therefore, we believe that the strategy demonstrated in this study could potentially boost the development of efficient catalysts towards the electrochemical oxidation of small molecules in general. Pristine Cu_2S NAs are also tested for HMF oxidation (Fig. S8†) and much lower anodic currents are observed. Besides, the Cu to Ni + Co ratio (full-range XPS spectra shown in Fig. S9a†) is determined to be ~1/9 after the electrodeposition, which implies that NiCo-LDHs are responsible for the outstanding activity. The electrodeposition time is optimized to be 450 s (Fig. S10†).

To identify the oxidation products and quantify the corresponding yields and faradaic efficiency, HMF oxidation catalyzed by $Cu_xS@Ni_{0.75}Co_{0.25}O_mH_n$ is performed at a fixed potential of 1.32 V *vs.* RHE and a total charge of ~58 C is passed.

The liquid samples are then collected after every 10 C of charge and analyzed by high-performance liquid chromatography (the spectra and corresponding calibration curves are shown in Fig. S11†). Fig. 3a shows the evolution of HPLC chromatogram traces, and the HMF/product concentration profile with increasing quantity of charge is plotted in Fig. 3b. A FDCA yield and faradaic efficiency of ~99% are obtained at the end of electrolysis, suggesting that $Cu_xS@Ni_{0.75}Co_{0.25}O_mH_n$ is

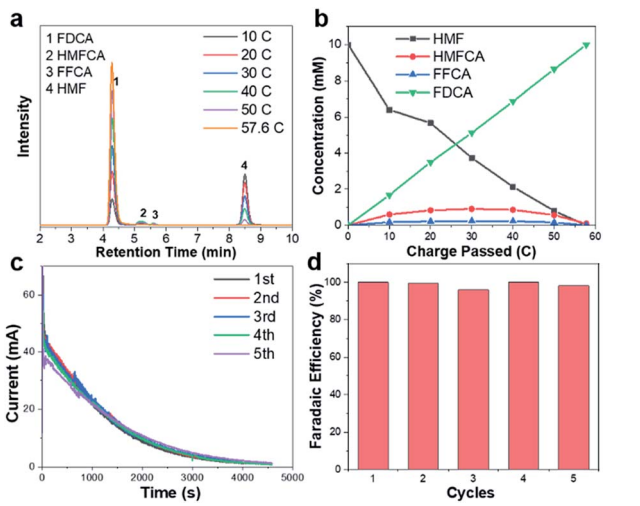

Fig. 3 (a) HPLC chromatogram traces of electrolyte during the electrochemical oxidation of HMF catalyzed by $Cu_xS@Ni_{0.75}Co_{0.25}O_mH_n$ at 1.32 V *vs.* RHE. (b) Concentration profiles of oxidation products with increasing charge. (c) Current–time curves and (d) faradaic efficiency towards FDCA in 5 successive runs.

highly active and selective under a potential as low as 1.32 V *vs.* RHE. Although the degradation of HMF under strong alkaline conditions has been reported, a highly active electrocatalyst could minimize this impact if HMF is quickly transformed to other chemicals. In the present study, ~50 C is passed in the first 35 min at 1.32 V *vs.* RHE and this corresponds to an HMF conversion of 87%. Therefore, the FDCA yield loss due to HMF degradation is negligible. The formation rate of HMFCA is higher in the initial period while no DFF is detected through the electrolysis, indicating that the oxidation of HMF might follow the pathway in which HMFCA is the oxidation intermediate towards FFCA (Scheme S1†).[13,24] The anodic scans of Cu_x-S@$Ni_{0.75}Co_{0.25}O_mH_n$ towards the oxidation of reaction intermediates (FFCA and HMFCA) are also collected and an onset potential similar to that of HMF is shown in Fig. S12;† this can be expected as the oxidation of hydroxyl and aldehyde functional groups follows the same Ni^{2+}/NiOOH pathway. The electrodes are further tested for 5 successive runs and the current–time curves show negligible degradation (Fig. 3c). The close-to-unity faradaic efficiency in all cases (Fig. 3d) also demonstrates their superior stability towards HMF oxidation.

To further address the effect of cobalt incorporation on the catalytic activity, we theoretically investigated the electronic structure of pristine NiOOH and NiCo-LDH with a Ni to Co ratio of 3. The projected density of states (Fig. 4a) shows the electronic states of the layered double hydroxide being modulated after Co participation. The electronic interaction between Co and Ni is further evidenced by the XPS (X-ray photoelectron spectroscopy) spectra of Cu_xS@NiO_mH_n and Cu_xS@$Ni_{0.75}Co_{0.25}O_mH_n$. The O 1s spectra of both samples are plotted in Fig. S9b† and the binding energy at 531.6 eV is assigned to the oxygen in the hydroxyl group.[25,42] As shown in the Ni $2p_{3/2}$ spectra (Fig. 4b), the binding energy of 855.6 eV in Cu_x-S@NiO_mH_n agrees well with that of nickel hydroxide.[42–44] The obvious positive shift (0.3 eV) of the Ni $2p_{3/2}$ peak in Cu_x-S@$Ni_{0.75}Co_{0.25}O_mH_n$ suggests a higher ratio of Ni^{3+}/Ni^{2+} when Co is present in the LDH.[45] As has been intensively studied in the oxygen evolution reaction, the occupancy of e_g orbitals in 3d transition-metal-based electrocatalysts is considered as a general activity descriptor.[46,47] The e_g orbital occupancy of close to 1 for surface metal ions could increase the covalency of the metal–oxygen bonds and is regarded as the optimal electronic configuration towards the adsorption/desorption of oxygen-containing reaction intermediates. Meanwhile, recent DFT calculations show that HMF molecules tend to be adsorbed on the surface of transition metal oxides by forming bonds between the metal cations and the formyl/hydroxyl oxygen atoms.[48] As illustrated in Fig. 4c, the Ni^{2+} is with a $t_{2g}^6e_g^2$ electronic configuration while Ni^{3+} possesses the $t_{2g}^6e_g^1$ configuration with a near-unity occupancy of the e_g orbital. Therefore, we anticipate that the tuned electronic structure of Ni could facilitate the adsorption of HMF on the electrode surface. At the present stage, it remains unclear whether or not the Co cation in mixed LDH is active towards oxidation of HMF. Nevertheless, as suggested by the recent *in situ* X-ray absorption spectroscopy measurements, the oxidation state of Co cation in NiCo mixed oxides remains nearly unchanged under applied electrochemical bias.[49,50] We then cautiously speculate that Ni acts as the dominant active sites in the mixed LDH whilst Co mainly promotes the oxidation of $Ni(OH)_2$ to NiOOH and facilitates HMF adsorption by modulating the electronic configuration of Ni. Furthermore, Boettcher *et al.* reported that the facile oxidation of NiCo-LDH can boost its electric conductivity by two orders of magnitude at ~1.2 V *vs.* RHE (compared with ~1.35 V *vs.* RHE for Ni hydroxide), indicating enhanced charge transfer in the mixed hydroxides.[51]

Based on the provided experimental evidence and discussion, we unambiguously attribute the superior HMF oxidation activity of the Cu_xS@$Ni_{0.75}Co_{0.25}O_mH_n$ to the following factors (Fig. 4d): (1) the transformation of $Cu(OH)_2$ to Cu_xS nanoarrays provides sufficient conductivity not only for the electrodeposition of ultra-thin NiCo-LDHs as active species but also for ensuring fast charge carrier transfer from the conductive substrate (Cu foam) to the surface of the shell catalytic layer; (2) the large surface area and open-channels of the core–shell nanostructure could expose a large number of active sites and also facilitate the mass transfer of reactants and products, assumably a more critical issue in HMF oxidation compared with O_2/H_2 evolution reaction where the gaseous products are neutrally charged and much easier to escape from the catalyst surface; (3) the tuned electronic structure of Ni due to Co incorporation represents an optimal construction where a higher content of Ni^{3+} with the e_g orbital occupancy close to 1 facilitates the adsorption of reactants and intermediates on the electrode surface and moreover, the oxidation of Ni^{2+} to NiOOH (which is the 'true' active species in HMF oxidation) occurs at significantly lower potentials compared with pristine $Ni(OH)_2$. Overall, the results presented herein demonstrate the synergy between nanostructure construction and electronic structure modulation to design more efficient electrocatalysts for

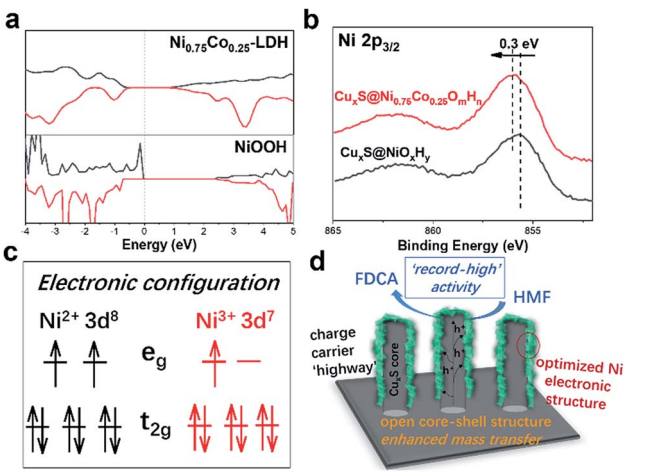

Fig. 4 (a) Projected density of states calculations for $Ni_{0.75}Co_{0.25}$-LDH and NiOOH. (b) High resolution Ni $2p_{3/2}$ XPS spectra of Cu_xS@$Ni_{0.75}Co_{0.25}O_mH_n$ and Cu_xS@NiO_mH_n. (c) Schematic illustration of the electronic configuration of the Ni cations with valence states of +2 and +3. (d) Schematic illustration of factors contributing to the high HMF oxidation activity.

biomass valorization and possibly other transition metal-catalyzed oxidation reactions.

As transition metal-based materials have been demonstrated in recent reports as efficient non-noble metal HER catalysts, it would be intriguing to integrate biomass valorization and H_2 production with a bifunctional electrocatalyst.[52–54] We thus evaluated the HER activity of Cu_xS@NiCo LDHs under alkaline conditions with a graphite rod as the counter electrode to avoid the possible contamination by Pt.[37,55–57] The LSV curves are shown in Fig. 5a. Apart from Cu_xS@CoO_mH_n, all the nickel containing composite electrodes show similar, yet outstanding HER activity. The overpotential to reach a current density of 10 mA cm^{-2} is in the range of 108–120 mV and such performance is comparable to those of the benchmark transition metal-based HER catalysts (Table S4†). The HER performance of Cu_xS@$Ni_{0.75}Co_{0.25}O_mH_n$ is then compared with those of bare Cu_xS, Pt mesh and $Ni_{0.75}Co_{0.25}O_mH_n$ deposited on Cu foam. As shown in the LSV curves (Fig. 5b) and Tafel plots (Fig. 5c), the Pt mesh demonstrates HER activity with an overpotential of 79 mV (@10 mA cm^{-2}) and a Tafel slope of 42 mV dec^{-1}, while Cu_xS@$Ni_{0.75}Co_{0.25}O_mH_n$ exhibits an overpotential of 107 mV and a remarkable Tafel slope of 35 mV dec^{-1}. In comparison, bare Cu_xS and $Ni_{0.75}Co_{0.25}O_mH_n$/CF show sluggish HER kinetics instead. Electrochemical impedance spectroscopy (EIS) is used to further compare the reaction kinetics. As plotted in Fig. S13,† Cu_xS@$Ni_{0.75}Co_{0.25}O_mH_n$ shows a much smaller charge transfer resistance of 5 Ω compared with bare Cu_xS and $Ni_{0.75}Co_{0.25}O_mH_n$/CF (~170 Ω) at −1.1 V *vs.* Hg/HgO, further demonstrating the significantly enhanced charge transfer in the core–shell nanoarray electrocatalyst. It should be noted that such HER performance enhancement cannot be solely explained by the contribution from the open nanostructure and larger number of exposed active sites. As suggested by the recent reports, we speculate that Cu–S–transition metal hydroxide interfaces might play a vital role in promoting water dissociation and facilitating the formation of H_{ad} intermediates in this case.[58,59] However, this requires more detailed investigation with additional theoretical insights, which will be studied further. The electrode exhibits an outstanding durability as the overpotential remains stable during 20 h of constant electrolysis (Fig. 5d) and the presence of HMF is found to have a negligible effect on the HER performance (Fig. 5e). The faradaic efficiency towards H_2 evolution is measured to be 100% (inset in Fig. 5e). Encouraged by the superior bifunctionality, an electrolyzer employing Cu_xS@$Ni_{0.75}Co_{0.25}O_mH_n$ as the cathode and anode is assembled and tested for simultaneous HMF oxidation and H_2 production. Impressively (Fig. 5f), the electrolyzer requires a mere 1.34 V to reach the current density of 10 mA cm^{-2} and 1.58 V to reach 100 mA cm^{-2}, which is ~270 mV less than that for the overall water splitting. Moreover, such performance is superior to those of other reported bifunctional electrocatalysts in light of the unique coupling of anodic oxidation reactions and H_2 production (Table S5†), further illustrating the effectiveness of the Cu_xS@NiCo-LDH nanoarray electrocatalysts.

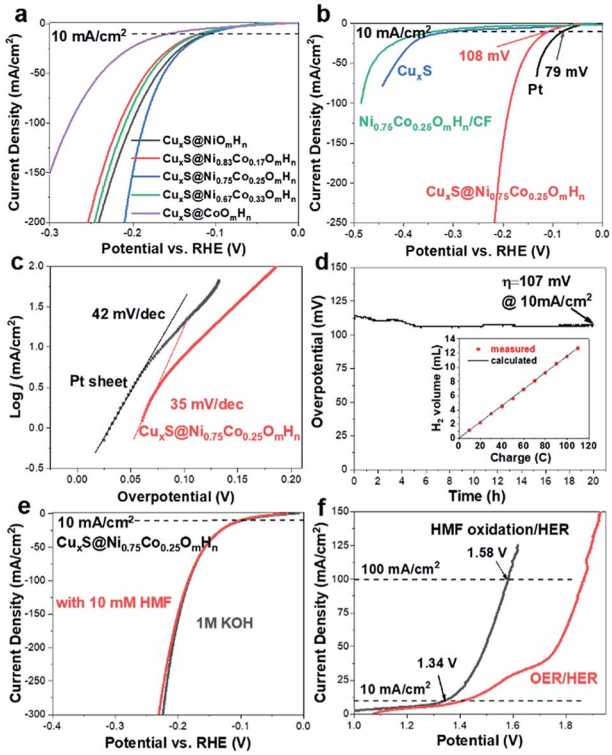

Fig. 5 HER curve comparison of (a) core–shell composites with various Ni and Co contents and (b) Cu_xS, Cu_xS@$Ni_{0.75}Co_{0.25}O_mH_n$, $Ni_{0.75}Co_{0.25}O_mH_n$/CF and Pt sheet (1 M KOH, pH 13.8; graphite rod as the counter electrode; 5 mV s^{-1}). (c) Tafel plots of Pt and Cu_xS@$Ni_{0.75}Co_{0.25}O_mH_n$ towards HER. (d) Stability test of Cu_xS@$Ni_{0.75}Co_{0.25}O_mH_n$ for 20 h (inset shows the faradaic efficiency towards H_2 evolution). (e) HER curve comparison of Cu_xS@$Ni_{0.75}Co_{0.25}O_mH_n$ in 1 M KOH with/without 10 mM HMF. (f) Comparison of LSV curves of overall water splitting and hydrogen evolution/HMF oxidation over the Cu_xS@$Ni_{0.75}Co_{0.25}O_mH_n$||Cu_xS@$Ni_{0.75}Co_{0.25}O_mH_n$ electrolyzer.

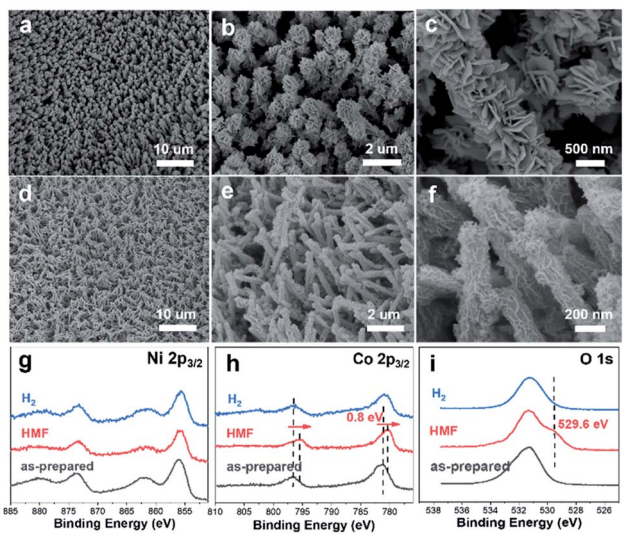

Fig. 6 SEM images of Cu_xS@$Ni_{0.75}Co_{0.25}O_mH_n$ after catalyzing long-term HMF oxidation (a–c) and HER (d–f). Ni $2p_{3/2}$ (g), Co $2p_{3/2}$ (h) and O 1s (i) XPS spectra of Cu_xS@$Ni_{0.75}Co_{0.25}O_mH_n$ after catalyzing long-term HMF oxidation (labeled as 'HMF') and hydrogen evolution reaction (labeled as 'H_2').

We further conducted detailed characterization on the electrodes after catalyzing long-term HMF oxidation and hydrogen evolution. As shown in the SEM images (Fig. 6), the nanoarray structure is maintained in both cases. However, it is noticed that the electrodeposited NiCo-LDH after HMF oxidation (Fig. 6a–c) turned into a dense layered structure with significantly increased thickness and such morphology is similar to the reported hydroxides before exfoliation.[60,61] This structural transformation is attributed to the phase cycling of metal hydroxides/oxyhydroxides during the oxidation of HMF, in which the transition metal hydroxides re-form at the end of each catalytic turnover. XPS results (Fig. 6g–i) show that the oxidation state of Ni remains unchanged after the stability test while an obvious negative shift (0.8 eV) of Co 2p spectra is observed along with a new peak appearing at 529.6 eV in O 1s spectra, which is then correlated with the formation of CoOOH species.[43] As pointed out earlier, Co catalyzes the HMF oxidation through a dominant direct oxidation pathway and the chemical oxidation (similar to the case of Ni) occurs at a much slower rate, it could therefore be expected that the oxidation state of Co after catalysis would be close to +3. On the other hand, SEM images (Fig. 6d–f) after the long-term HER test show that the previous 3D core–shell nanostructure is maintained with little aggregation and the high-resolution Ni 2p, Co 2p and O 1s XPS spectra are nearly identical to that of the as-prepared sample. The leaching of transition metal species after catalyzing long-term HER and HMF oxidation is investigated by ICP-OES. It is shown that the content of Ni and Co (as active species) in the electrolyte in both cases is below the detection limit (0.02 mg L^{-1}) while the Cu leaching is more severe as 0.12 mg L^{-1} and 11.03 mg L^{-1} of Cu are detected after catalyzing HER and HMF oxidation. The much higher leaching of Cu in the case of HMF oxidation corresponds to a leached Cu amount of 0.17 mg cm^{-2} and is attributed to the oxidation/dissolution of exposed Cu_xS species under anodic conditions. Nevertheless, the electrochemical stability test and post-SEM characterization show that such leaching has a negligible effect on the performance and structural stability of core–shell nanoarrays.

4. Conclusions

To summarize, Cu_xS@NiCo-LDHs nanoarrays are facilely fabricated as efficient bifunctional electrocatalysts towards HMF oxidation and H_2 generation. Owing to the superior conductivity of the copper sulfide core, the modulated electronic structure, the redox behavior of Ni in the catalyst layer and the nanowire@nanosheet open structure which greatly facilitates the mass transfer and exposes a large number of active sites, the optimized catalysts exhibit superior electrocatalytic activity/durability towards HMF oxidation and H_2 evolution. Moreover, the faradaic efficiency towards FDCA and H_2 is close to unity. With the outstanding bifunctionality, the two-electrode electrolyzer only requires a voltage of 1.34 V to achieve simultaneous biomass upgrading and H_2 generation at the current density of 10 mA cm^{-2}. Our study significantly advances research towards Ni-catalyzed biomass upgrading and more efficient H_2 production from aqueous solution.

Conflicts of interest

There are no conflicts to declare.

Acknowledgements

This work is financially supported by the National Natural Science Foundation of China (No. 21905181 and 21975163) and China Postdoctoral Science Foundation (No. 2018M633125). The authors acknowledge Dr Wenguang Zhao from Peking University, Shenzhen Graduate School for the TEM analysis. We are also grateful to Dr Lin Lin and Materials Characterization & Preparation Center of Southern University of Science and Technology for HPLC measurements.

Notes and references

1 L. Han, S. J. Dong and E. K. Wang, *Adv. Mater.*, 2016, **28**, 9266–9291.
2 I. Roger, M. A. Shipman and M. D. Symes, *Nat. Rev. Chem.*, 2017, **1**, 1–13.
3 T. W. Kim and K. S. Choi, *Science*, 2014, **343**, 990–994.
4 F. Yu, L. Yu, I. K. Mishra, Y. Yu, Z. F. Ren and H. Q. Zhou, *Materials Today Physics*, 2018, **7**, 121–138.
5 C. C. L. McCrory, S. Jung, I. M. Ferrer, S. M. Chatman, J. C. Peters and T. F. Jaramillo, *J. Am. Chem. Soc.*, 2015, **137**, 4347–4357.
6 B. You, X. Liu, N. Jiang and Y. Sun, *J. Am. Chem. Soc.*, 2016, **138**, 13639–13646.
7 Y. Huang, X. D. Chong, C. B. Liu, Y. Liang and B. Zhang, *Angew. Chem., Int. Ed.*, 2018, **57**, 13163–13166.
8 L. Du, Y. Y. Shao, J. M. Sun, G. P. Yin, C. Y. Du and Y. Wang, *Catal. Sci. Technol.*, 2018, **8**, 3216–3232.
9 J.-Y. Zhang, H. Wang, Y. Tian, Y. Yan, Q. Xue, T. He, H. Liu, C. Wang, Y. Chen and B. Y. Xia, *Angew. Chem., Int. Ed.*, 2018, **57**, 7649–7653.
10 G.-F. Chen, Y. Luo, L.-X. Ding and H. Wang, *ACS Catal.*, 2018, **8**, 526–530.
11 Q. Zhou, Z. Shen, C. Zhu, J. Li, Z. Ding, P. Wang, F. Pan, Z. Zhang, H. Ma, S. Wang and H. Zhang, *Adv. Mater.*, 2018, 1800140.
12 G. Wang and Z. Wen, *Nanoscale*, 2018, **10**, 21087–21095.
13 B. You, N. Jiang, X. Liu and Y. Sun, *Angew. Chem., Int. Ed.*, 2016, **55**, 9913–9917.
14 N. Jiang, B. You, R. Boonstra, I. M. Terrero Rodriguez and Y. Sun, *ACS Energy Lett.*, 2016, **1**, 386–390.
15 B. J. Taitt, D.-H. Nam and K.-S. Choi, *ACS Catal.*, 2019, **9**, 660–670.
16 S. R. Kubota and K. S. Choi, *ChemSusChem*, 2018, **11**, 2138–2145.
17 W. J. Liu, L. N. Dang, Z. R. Xu, H. Q. Yu, S. Jin and G. W. Huber, *ACS Catal.*, 2018, **8**, 5533–5541.
18 M. E. Zakrzewska, E. Bogel-Łukasik and R. Bogel-Łukasik, *Chem. Rev.*, 2011, **111**, 397–417.
19 H. A. Rass, N. Essayem and M. Besson, *ChemSusChem*, 2015, **8**, 1206–1217.

20 B. Siyo, M. Schneider, J. Radnik, M. M. Pohl, P. Langer and N. Steinfeldt, *Appl. Catal., A*, 2014, **478**, 107–116.
21 H. G. Cha and K. S. Choi, *Nat. Chem.*, 2015, **7**, 328–333.
22 M. Fleischmann, K. Korinek and D. J. Pletcher, *J. Chem. Soc., Perkin Trans. 2*, 1972, (10), 1396–1403.
23 M. Fleischmann, K. Korinek and D. J. Pletcher, *J. Electroanal. Chem. Interfacial Electrochem.*, 1971, **31**, 39–49.
24 S. Barwe, J. Weidner, S. Cychy, D. M. Morales, S. Dieckhöfer, D. Hiltrop, J. Masa, M. Muhler and W. Schuhmann, *Angew. Chem., Int. Ed.*, 2018, **57**, 11460–11464.
25 Q. H. Zhao, J. L. Yang, M. Q. Liu, R. Wang, G. X. Zhang, H. Wang, H. T. Tang, C. K. Liu, Z. W. Mei, H. B. Chen and F. Pan, *ACS Catal.*, 2018, **8**, 5621–5629.
26 Y. Zhao, X. Zhang, X. Jia, G. I. N. Waterhouse, R. Shi, X. Zhang, F. Zhan, Y. Tao, L.-Z. Wu, C.-H. Tung, D. O'Hare and T. Zhang, *Adv. Energy Mater.*, 2018, **8**, 1703585.
27 G. Kresse and J. Furthmüller, *Phys. Rev. B: Condens. Matter Mater. Phys.*, 1996, **54**, 11169–11186.
28 G. Kresse and J. Hafner, *Phys. Rev. B: Condens. Matter Mater. Phys.*, 1994, **49**, 14251–14269.
29 P. E. Blöchl, *Phys. Rev. B: Condens. Matter Mater. Phys.*, 1994, **50**, 17953–17979.
30 J. P. Perdew, K. Burke and M. Ernzerhof, *Phys. Rev. Lett.*, 1996, **77**, 3865–3868.
31 S. L. Dudarev, G. A. Botton, S. Y. Savrasov, C. J. Humphreys and A. P. Sutton, *Phys. Rev. B: Condens. Matter Mater. Phys.*, 1998, **57**, 1505–1509.
32 X. H. Xia, C. R. Zhu, J. S. Luo, Z. Y. Zeng, C. Guan, C. F. Ng, H. Zhang and H. J. Fan, *Small*, 2014, **10**, 766–773.
33 M. S. Burke, L. J. Enman, A. S. Batchellor, S. H. Zou and S. W. Boettcher, *Chem. Mater.*, 2015, **27**, 7549–7558.
34 B. Liu, S. X. Qu, Y. Kou, Z. Liu, X. Chen, Y. T. Wu, X. P. Han, Y. D. Deng, W. B. Hu and C. Zhong, *ACS Appl. Mater. Interfaces*, 2018, **10**, 30433–30440.
35 L. L. Feng, M. H. Fan, Y. Y. Wu, Y. P. Liu, G. D. Li, H. Chen, W. Chen, D. J. Wang and X. X. Zou, *J. Mater. Chem. A*, 2016, **4**, 6860–6867.
36 X. Long, G. X. Li, Z. L. Wang, H. Y. Zhu, T. Zhang, S. Xiao, W. Y. Guo and S. H. Yang, *J. Am. Chem. Soc.*, 2015, **137**, 11900–11903.
37 L. Yu, H. Q. Zhou, J. Y. Sun, F. Qin, F. Yu, J. M. Bao, Y. Yu, S. Chen and Z. F. Ren, *Energy Environ. Sci.*, 2017, **10**, 1820–1827.
38 J. Hou, Y. Wu, B. Zhang, S. Cao, Z. Li and L. Sun, *Adv. Funct. Mater.*, 2019, 1808367.
39 J. Weidner, S. Barwe, K. Sliozberg, S. Piontek, J. Masa, U. P. Apfel and W. Schuhmann, *Beilstein J. Org. Chem.*, 2018, **14**, 1436–1445.
40 L. Trotochaud, S. L. Young, J. K. Ranney and S. W. Boettcher, *J. Am. Chem. Soc.*, 2014, **136**, 6744–6753.
41 Z.-Y. Yu, C.-C. Lang, M.-R. Gao, Y. Chen, Q.-Q. Fu, Y. Duan and S.-H. Yu, *Energy Environ. Sci.*, 2018, **11**, 1890–1897.
42 X. H. Deng, S. Ozturk, C. Weidenthaler and H. Tuysuz, *ACS Appl. Mater. Interfaces*, 2017, **9**, 21225–21233.
43 N. S. McIntyre and M. G. Cook, *Anal. Chem.*, 1975, **47**, 2208–2213.
44 A. P. Grosvenor, M. C. Biesinger, R. S. Smart and N. S. McIntyre, *Surf. Sci.*, 2006, **600**, 1771–1779.
45 S. H. Ye, Z. X. Shi, J. X. Feng, Y. X. Tong and G. R. Li, *Angew. Chem., Int. Ed.*, 2018, **57**, 2672–2676.
46 J. Suntivich, K. J. May, H. A. Gasteiger, J. B. Goodenough and Y. Shao-Horn, *Science*, 2011, **334**, 1383–1385.
47 Y. Zhao, X. Jia, G. Chen, L. Shang, G. I. N. Waterhouse, L.-Z. Wu, C.-H. Tung, D. O'Hare and T. Zhang, *J. Am. Chem. Soc.*, 2016, **138**, 6517–6524.
48 J. Ren, K. H. Song, Z. Li, Q. Wang, J. Li, Y. X. Wang, D. B. Li and C. K. Kim, *Appl. Surf. Sci.*, 2018, **456**, 174–183.
49 H. Y. Wang, Y. Y. Hsu, R. Chen, T. S. Chan, H. M. Chen and B. Liu, *Adv. Energy Mater.*, 2015, **5**, 1500091.
50 M. K. Bates, Q. Jia, H. Doan, W. Liang and S. Mukerjee, *ACS Catal.*, 2016, **6**, 155–161.
51 M. B. Stevens, L. J. Enman, E. H. Korkus, J. Zaffran, C. D. M. Trang, J. Asbury, M. G. Kast, M. C. Toroker and S. W. Boettcher, *Nano Res.*, 2019, **12**, 2288–2295.
52 F. Yu, H. Zhou, Y. Huang, J. Sun, F. Qin, J. Bao, W. A. GoddardIII, S. Chen and Z. Ren, *Nat. Commun.*, 2018, **9**, 2551.
53 J. Sun, M. Ren, L. Yu, Z. Yang, L. Xie, F. Tian, Y. Yu, Z. Ren, S. Chen and H. Zhou, *Small*, 2019, **15**, 1804272.
54 J. Zhang, T. Wang, P. Liu, Z. Liao, S. Liu, X. Zhuang, M. Chen, E. Zschech and X. Feng, *Nat. Commun.*, 2017, **8**, 15437.
55 X. Wang, Y. Yang, L. Diao, Y. Tang, F. He, E. Liu, C. He, C. Shi, J. Li, J. Sha, S. Ji, P. Zhang, L. Ma and N. Zhao, *ACS Appl. Mater. Interfaces*, 2018, **10**, 35145–35153.
56 Y. Zhou, Z. Wang, Z. Pan, L. Liu, J. Xi, X. Luo and Y. Shen, *Adv. Mater.*, 2019, **31**, 18067690.
57 R. Chen, C. J. Yang, W. Z. Cai, H. Y. Wang, J. W. Miao, L. P. Zhang, S. L. Chen and B. Liu, *ACS Energy Lett.*, 2017, **2**, 1070–1075.
58 Y. Liu, Q. Li, R. Si, G.-D. Li, W. Li, D.-P. Liu, D. Wang, L. Sun, Y. Zhang and X. X. Zou, *Adv. Mater.*, 2017, **29**, 1606200.
59 J.-X. Feng, J.-Q. Wu, Y.-X. Tong and G.-R. Li, *J. Am. Chem. Soc.*, 2018, **140**, 610–617.
60 M. Gao, W. Sheng, Z. Zhuang, Q. Fang, S. Gu, J. Jiang and Y. Yan, *J. Am. Chem. Soc.*, 2014, **136**, 7077–7084.
61 F. Song and X. Hu, *Nat. Commun.*, 2014, **5**, 4477.